Traction reveals mechanisms of wall effects for microswimmers near boundaries

Xinhui Shen, Marcos, and Henry C. Fu

Phys. Rev. E **95**, 033105 — Published 9 March 2017

DOI: 10.1103/PhysRevE.95.033105

Traction Reveals Mechanisms of Wall-effects for Microswimmers near Boundaries

Xinhui Shen,[1] Marcos,[1,*] and Henry C. Fu[2,*]

[1] *School of Mechanical and Aerospace Engineering, Nanyang Technological University, Singapore*
[2] *Department of Mechanical Engineering, University of Utah, Salt Lake City, Utah 84112, USA*

(Dated: February 13, 2017)

The influence of a plane boundary on low-Reynolds number swimmers has frequently been studied using image systems for flow singularities. However, the boundary effect can also be expressed using a boundary integral representation over the traction on the boundary. We show that examining the traction pattern on the boundary caused by a swimmer can yield physical insights into determining when far-field multipole models are accurate. We investigate the swimming velocities and the traction of a three-sphere swimmer initially placed parallel to an infinite planar wall. In the far-field, the instantaneous effect of the wall on the swimmer is well-approximated by that of a multipole expansion consisting of a force dipole and a force quadrupole. On the other hand, the swimmer close to the wall must be described by a system of singularities reflecting its internal structure. We show that these limits and the transition between them can be independently identified by examining the traction pattern on the wall, either using a quantitative correlation coefficient or by visual inspection. Last, we find that for non-constant propulsion, correlations between swimming stroke motions and internal positions are important and not captured by time-averaged traction on the wall, indicating that care must be taken when applying multipole expansions to study boundary effects in cases of non-constant propulsion.

I. INTRODUCTION

The propulsion of microscopic organisms and engineered structures has been an area of recent interest. Microorganisms play an active role in nature [1–3], and many species swim through fluids. For example, a bacterium rotates its helical flagella [4] while a sperm propagates traveling wave on its flagellum [5–7] in order to achieve a forward motion. Artificial microrobots capable of propulsion in fluids have also been studied and fabricated [8–16] with many potential applications, such as microsurgery [17, 18] and drug delivery [19, 20]. To understand how microscale locomotion can be achieved, one can use simplified models of microscale propulsion, including the Taylor Sheet [21–23], Purcell's 3-link swimmer [24], the three-sphere swimmer [25, 26] and the two-sphere swimmer [27].

In the low Reynolds number regime encountered by microswimmers, fluid dynamics are governed by the Stokes equation. Due to the linearity of the Stokes equation, a profitable approach to understand the behavior of microorganisms is to construct flow solutions as the superposition of a discrete set of or continuous distribution of fundamental singular solutions, such as the Stokeslet, which is the flow due to a point force acting on the fluid [28]. For instance, a bacterial flagellum can be modeled by a distribution of Stokeslets and Stokeslet dipoles [29, 30], or the entire swimmer can be modeled by a surface distribution of singular solutions [31] or a collection of regularized solutions [32–36]. Reduced order models composed of a discrete set of singular solutions have also been useful, such as for *Chlamydomonas* [37]. Insight into the flows around swimming organisms can also be obtained by adopting the far field approximation of a multipole expansion [28, 38]. The induced flow field of a bacterium at large distances decays as r^{-2}, indicating that it can also be treated as a force dipole in the far field [39–41]. Similarly, in the far field, a swimming spermatozoa can be modeled as a combination of Stokeslet dipole and quadrupole [42]. The far field character can also be altered upon time-averaging. For example, the flow induced by a three-sphere swimmer modeled as three Stokeslets switches from dipolar to quadrupolar upon time-averaging [43].

Since microswimmers often swim in confined spaces near boundaries, there is interest in understanding the effects of boundaries on swimming [44–51]. In this case, it has also been useful to employ singularity approaches and far-field multipole expansions [50, 52, 53]. In the presence of a boundary, the image system method [54] can be applied to satisfy the no-slip boundary conditions for singular solutions. Spagnolie *et al.* [55] have shown that for large distances from the boundary, a far-field multipole expansion and its image system can accurately predict the effects of boundaries on pitching movements for swimmers with steady propulsion mechanisms. However, they find that the closest approach to the boundary for which the approach is valid depends on geometry and mode of propulsion of the swimmer, and could range from tenths of body lengths to approximately a single body length, with no a priori way of determining the range of validity.

Here, we take advantage of the fact that the Lorentz reciprocal theorem implies that the flow field induced by a particular singularity and its images can also be expressed in terms of the traction exerted by the boundary on the fluid [28, 56]. This is analogous to how in electrostatics the electric field near a conductor

* Corresponding Authors: marcos@ntu.edu.sg, henry.fu@utah.edu

can be represented using either image charges or a charge distribution on the conducting surface. The image system method is usually simpler and the more common approach but we suggest that examining the traction on the boundary can give additional insight into boundary effects that are harder to access by the image system approach.

In this article, we theoretically analyse the spatial pattern of traction on the wall induced by a swimmer in vicinity of an infinite planar wall. We use a three-sphere swimmer [25] initially placed parallel to the wall. We obtain exact solutions using the image system method to find the instantaneous forces acting on the three spheres and the instantaneous velocity of the swimmer. As a function of distance from the wall, we identify when far-field approximations of the swimmer based on multipole expansions and image velocity fields are appropriate to describe the effect of the boundary. We then evaluate the distribution of traction on the wall and show that examining the traction pattern gives insight into whether the far field approximation applies, or, in contrast, the internal structure of the swimmer must be taken into account. Thus the traction provides an independent way to check and understand when the multipole expansion is valid. We discuss the effect of time-averaging on our results. The conclusions should be generalizable to more realistic swimmers in addition to the three-sphere swimmer.

II. SWIMMER MODEL

For a low-Reynolds number swimmer swimming in vicinity of a planar wall, conventional methods apply the image system approach to solve for the forces acting on a swimmer and the flow field generated by the swimmer. For a three-sphere swimmer, we follow Zargar *et al.* [57] to find swimming velocities using the image system approach. Using the same method, we generate solutions for traction. We then compare this method to a method that relies solely on the traction on the wall, and analyze the traction patterns for insights.

We consider a three-sphere swimmer [25] with spheres of equal radius a swimming in a fluid with viscosity μ near an infinite planar wall at $x_1 = 0$ (FIG. 1). The three spheres from left to right are labeled as sphere 1, 2 and 3, respectively, and the prescribed lengths of the left and right arm, l^{12} and l^{23}, are,

$$l^{12}(t) = L + \zeta\cos(\omega t), \tag{1}$$
$$l^{23}(t) = L + \zeta\cos(\omega t + \phi). \tag{2}$$

Initially, the swimmer is placed parallel to and at a distance h from the infinite wall. In this paper we nondimensionalize all physical parameters using the viscosity μ, the angular frequency ω and the characteristic length of the swimmer L. For example, the nondimensionalized arm length $\tilde{l}^{12} = 1 + \tilde{\zeta}\cos(t)$. For convenience, in the remainder of the paper, we drop tildes and all variables refer to dimensionless quantities unless otherwise specified. All results presented are for sphere radii $a = 0.01$, amplitude of the harmonic motion $\zeta = 0.1$, and phase angle $\phi = \pi/2$. For $a \ll 1$ and as long as $a \ll h$, each sphere can be modeled as a Stokeslet placed at its geometric center. Note that we set the axis of the swimmer to coincide with the plane $x_3 = 0$ so that the swimmer's motion remains in the x_2-x_1 plane.

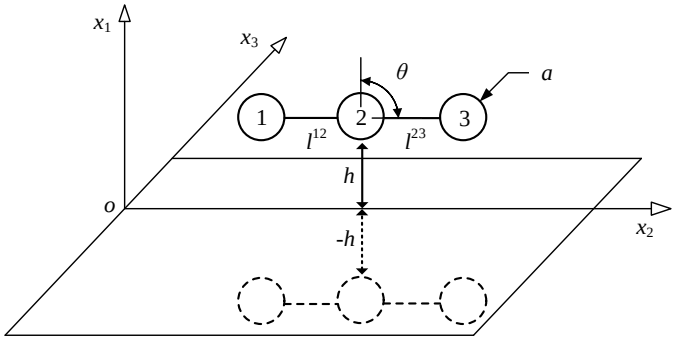

FIG. 1. A three-sphere swimmer and its image system with respect to an infinite planar wall. Spheres with radius a are labeled $\alpha = 1, 2, 3$ from left to right. The two arms l^{12} and l^{23} perform periodic motions. Initially, the swimmer is placed parallel to the wall ($\theta = \pi/2$).

The position of each sphere can be related to the center of mass (CM) of the swimmer $\mathbf{x}^0$,

$$\begin{bmatrix} x_1^\alpha \\ x_2^\alpha \end{bmatrix} = \begin{bmatrix} x_1^0 \\ x_2^0 \end{bmatrix} + G^\alpha \begin{bmatrix} \cos\theta \\ \sin\theta \end{bmatrix}, \tag{3}$$

where $\mathbf{x}$ is the position vector, the superscript $\alpha = 1, 2, 3$ represents the sphere number, subscripts denote directional components, and

$$G^\alpha = \begin{cases} \left(-2l^{12} - l^{23}\right)/3, & \alpha = 1 \\ \left(l^{12} - l^{23}\right)/3, & \alpha = 2 \\ \left(l^{12} + 2l^{23}\right)/3, & \alpha = 3 \end{cases}. \tag{4}$$

Differentiating Eq. 3 relates the velocity of each sphere, $\mathbf{v}^\alpha$ to the swimmer's velocity $\mathbf{v}^0$, rotation rate $\dot{\theta}$, and arm lengths l:

$$\begin{bmatrix} v_1^\alpha \\ v_2^\alpha \end{bmatrix} = \begin{bmatrix} v_1^0 \\ v_2^0 \end{bmatrix} + \begin{bmatrix} -\sin\theta \\ \cos\theta \end{bmatrix} \dot{\theta} G^\alpha + \begin{bmatrix} \cos\theta \\ \sin\theta \end{bmatrix} \dot{G}^\alpha. \tag{5}$$

To find the velocity of the swimmer, we utilize the Blakeslet [54] which is the solution to a point force acting on a fluid in the presence of a no-slip boundary [57]. The Blakeslet consists of a Stokeslet (**S**) and a set of images (**St**) placed below the boundary, which are explicitly defined in Appendix A. Following the conventions of Appendix A, the velocity of sphere α can be represented as,

$$v_i^\alpha = \sum_{\beta=1}^{3} \left[S_{ij}(\mathbf{x}^\alpha, \mathbf{x}^\beta) + St_{ij}(\mathbf{x}^\alpha, \mathbf{x}^{\beta *})\right] f_j^\beta. \tag{6}$$

where $\mathbf{f}^\beta$ is the force acting on sphere β, $\mathbf{x}^\beta$ is the Stokeslet location and $\mathbf{x}^{\beta*}$ the corresponding image location.

Since inertia is negligible at low Reynolds number, the total force and torque acting on the three-sphere swimmer are zero,

$$\sum_{\beta=1}^{3} \mathbf{f}^\beta = 0, \tag{7}$$

$$\sum_{\beta=1}^{3} -G^\beta \sin\theta f_1^\beta + G^\beta \cos\theta f_2^\beta = 0. \tag{8}$$

Eqs. 3 - 8 are a linear system which can be solved to obtain $\mathbf{v}^0$, $\mathbf{v}^\alpha$ and $\mathbf{f}^\beta$.

In the following we decompose the total velocity of the swimmer into two parts, $\mathbf{v}^0 = \mathbf{v}^{0*} + \mathbf{u}^{0*}$. The first is due to the three Stokeslets,

$$v_i^{0*} = \frac{1}{3}\sum_{\alpha\beta} \left[S_{ij}(\mathbf{x}^\alpha, \mathbf{x}^\beta)\right] f_j^\beta, \tag{9}$$

and the other due to their corresponding images, which we call the wall-induced swimming velocity,

$$u_i^{0*} = \frac{1}{3}\sum_{\alpha\beta} \left[St_{ij}(\mathbf{x}^\alpha, \mathbf{x}^{\beta*})\right] f_j^\beta, \tag{10}$$

On the other hand, in the absence of the wall, the velocity of the free swimmer can be expressed as,

$$v_i^{0,\mathrm{free}} = \frac{1}{3}\sum_{\alpha\beta} \left[S_{ij}(\mathbf{x}^\alpha, \mathbf{x}^\beta)\right] f_j^{\beta,\mathrm{free}}. \tag{11}$$

The change in swimming velocity due to the wall, $\mathbf{v}^0 - \mathbf{v}^{0,\mathrm{free}}$, is not precisely equal to $\mathbf{u}^{0*}$ because the forces $\mathbf{f}^\beta$ differ from $\mathbf{f}^{\beta,\mathrm{free}}$. However, they are quite close, meaning that most of the change in velocity is caused by the wall-induced velocity rather than changes in the internal forces of the swimmer (FIG. 2). Thus, in the following we concentrate on how well the wall-induced velocity $\mathbf{u}^{0*}$ can be approximated by a far field approach, and how that is reflected in the traction. Last we define the wall-induced velocity field at any point $\mathbf{x}^\mathrm{p}$, calculated as

$$u_i^*(\mathbf{x}^\mathrm{p}) = \sum_{\beta=1}^{3} St_{ij}\left(\mathbf{x}^\mathrm{p}, \mathbf{x}^{\beta*}\right) f_j^\beta. \tag{12}$$

The image system method is analogous to that used in electrostatics to find electric fields near conducting planes. In the electrostatic case, the field is physically produced by the combined effect of the original charge and the surface charge distribution on the conductor. Similarly, in the hydrodynamic case, the wall-induced velocity can be represented as that due to a force distribution (traction) on the boundary, which is the wall's portion of the single-layer representation of the velocity field [56]. Details are written explicitly in Appendix B, but to summarize, in our case we first evaluate the traction on the wall $\mathbf{x}^\mathrm{w}$ due to a Blakeslet at $\mathbf{x}^\beta$ with force $\mathbf{f}^\beta$, which we write as $\tau_{ij}(\mathbf{x}^\mathrm{w}, \mathbf{x}^\beta) f_j^\beta$. For three spheres with forces $\mathbf{f}^\beta$ the traction at $\mathbf{x}^\mathrm{w}$ induced by the three sphere swimmer can be obtained as,

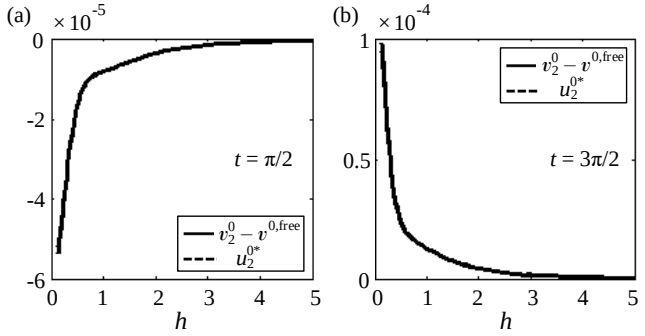

FIG. 2. The change in swimming velocity due to the wall (solid line), $v_2^0 - v^{0,\mathrm{free}}$, and the wall-induced velocity (dashed line), u_2^{0*}, versus the (nondimensional) initial distance from the wall at (a) $t = \pi/2$ and (b) $t = 3\pi/2$. Note that both lines coincide.

$$T_i(\mathbf{x}^\mathrm{w}) = \sum_{\beta=1}^{3} \tau_{ij}(\mathbf{x}^\mathrm{w}, \mathbf{x}^\beta) f_j^\beta. \tag{13}$$

Further substituting $\mathbf{T}(\mathbf{x}^\mathrm{w})$ into Eq.(B13) allows us to evaluate the flow field at $\mathbf{x}^\mathrm{p}$ by integrating the flow produced by the traction forces acting over the entire wall surface S,

$$u_i^*(\mathbf{x}^\mathrm{p}) = \int_S S_{ij}\left(\mathbf{x}^\mathrm{p}, \mathbf{x}^\mathrm{w}\right) T_j\left(\mathbf{x}^\mathrm{w}\right) dS. \tag{14}$$

This is an alternative way to compute the result of Eq. 12, and suggests that analyzing the traction will give insight into the nature of the effect of the wall on swimming velocities.

III. INSTANTANEOUS RESPONSE

In this section, we use the image system method to calculate the swimming velocity of the swimmer as a function of the distance from the wall, then analyze the wall contribution in terms of a multipole expansion. Comparing the two we determine when the multipole expansion is valid, and the internal structure of the swimmer can be ignored. Then we turn to the traction, and show that the range of validity of the multipole expansion can be independently determined by observing when the spatial pattern of the traction resembles those expected from pure multipoles.

The image system method follows the results reported by Zargar *et al.* [57]. To analyse the instantaneous

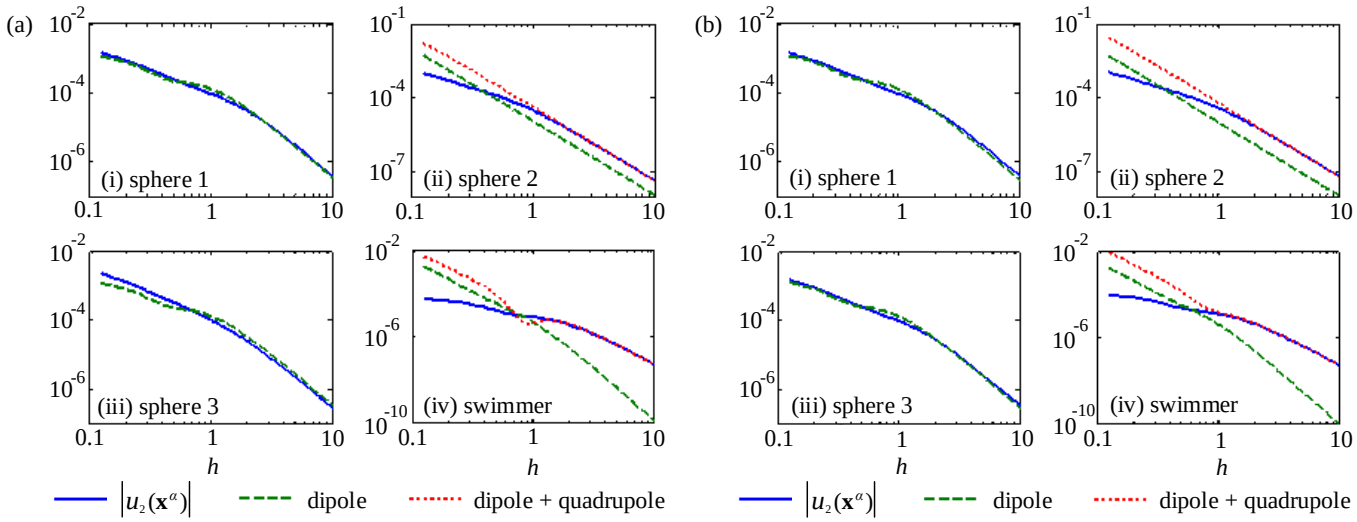

FIG. 3. (color online) The log-log plots of the magnitude of velocities versus the (nondimensional) initial distance from the wall at (a) $t = \pi/2$ and (b) $t = 3\pi/2$. The solid blue line represents the exact wall-induced velocity of (i) sphere 1, (ii) sphere 2, (iii) sphere 3, and (iv) the swimmer. The dashed green line represents the corresponding dipolar model. The dotted red line represents the corresponding combination of the dipole and quadrupole model.

flow field, we set our point of interest $\mathbf{x}^{\mathrm{p}}$ to be at the instantaneous positions of the three spheres $\mathbf{x}^\alpha$. The average of the three velocities at these positions yields the instantaneous flow velocity at the CM of the swimmer due to its image system $\mathbf{u}^{0*}$. Our focus is the instantaneous velocity along the x_2 direction since $u_2^*(\mathbf{x}^\alpha)$ is significantly larger than the translational velocity in the x_1 direction and the rotational velocity. Since both forces on three spheres and sphere positions vary with time, the magnitude of wall-induced velocities and the multipole expansions both vary over a cycle. However, at all times we checked throughout the cycle we find the behavior described below; as representative examples we plot the x_2 component of the instantaneous wall-induced velocities $u_2^*(\mathbf{x}^\alpha)$ and u_2^{0*} at two time points $t = \pi/2$ and $t = 3\pi/2$ are shown in FIG. 3 (solid blue lines).

We perform a multipole expansion on Eq. 12 by defining $\mathbf{d}^{\beta*} = \mathbf{x}^{\beta*} - \mathbf{x}^{0*}$ as the image displacement vector from the image CM of the swimmer to the image sphere β. The expansion is expected to be valid when the swimmer is far away from the wall, or $|\mathbf{x}^\alpha - \mathbf{x}^{0*}| \gg |\mathbf{d}^{\beta*}|$ for any α, β. Performing a Taylor expansion around the image CM of the swimmer we obtain,

$$\begin{aligned} u_i^*(\mathbf{x}^\alpha) = &\sum_{\beta=1}^{3} St_{ij}\left(\mathbf{x}^\alpha, \mathbf{x}^{0*}\right) f_j^\beta \\ &+ \partial_k St_{ij}\left(\mathbf{x}^\alpha, \mathbf{x}^{0*}\right) f_j^\beta d_k^{\beta*} \\ &+ \partial_l \partial_k St_{ij}\left(\mathbf{x}^\alpha, \mathbf{x}^{0*}\right) f_j^\beta d_k^{\beta*} d_l^{\beta*}, \end{aligned} \tag{15}$$

where the derivatives act on the second argument of $\mathbf{St}$. The first three terms in the expansion represent the wall contribution of a Stokeslet, a Stokeslet dipole and a Stokeslet quadrupole, respectively. The first term vanishes since the swimmer is force-free, so the subsequent dipolar term is the leading order contribution to the wall-induced velocity. As seen from FIG. 3a,b in panels (i) and (iii) (dashed green lines), the dipole model matches well with the actual wall-induced velocity (solid blue lines) at $\mathbf{x}^1$ and $\mathbf{x}^3$ for $h > 2$, which indicates that the image system of a three-sphere swimmer at a large distance to the wall is well-represented by that of a Stokeslet dipole. However, the velocity $\mathbf{u}^*(\mathbf{x}^2)$ is much smaller than $\mathbf{u}^*(\mathbf{x}^1)$ or $\mathbf{u}^*(\mathbf{x}^3)$ (note vertical scale on FIG. 3a,b panels (ii)). This is due to the fact that $\mathbf{x}^2 - \mathbf{x}^{0*}$ and the image displacement vectors $\mathbf{d}^{\beta*}$ are almost perpendicular to the forces $\mathbf{f}^\beta$, and the wall-induced velocity of a dipole image vanishes in that direction. Therefore the subsequent term in the multipole expansion, the quadrupole, is needed to accurately describe the actual wall-induced velocity for sphere 2 (FIG. 3a,b panels (ii)).

The wall-induced contribution to the CM swimming velocity (FIG. 3a,b panels (iv)) is the average of the wall-induced velocities of the three spheres. The dipolar wall-induced CM swimming velocity nearly vanishes because the contribution of sphere 2 is negligible and the contributions of sphere 1 and 3 nearly cancel: $\mathbf{x}^1$ and $\mathbf{x}^3$ are almost symmetric about $\mathbf{x}^0$ but the x_2-component of the dipolar velocity is odd in the x_2 direction. Therefore, the multipole expansion of the CM swimming velocity requires the quadrupolar term to be accurate. At a given distance from the wall, the instantaneous validity of the multipole expansion holds for all times during the cycle. In summary, the multipole expansion is valid for $h > 2$ both for individual spheres and the CM velocity, as long as both dipole and quadrupole contributions are included.

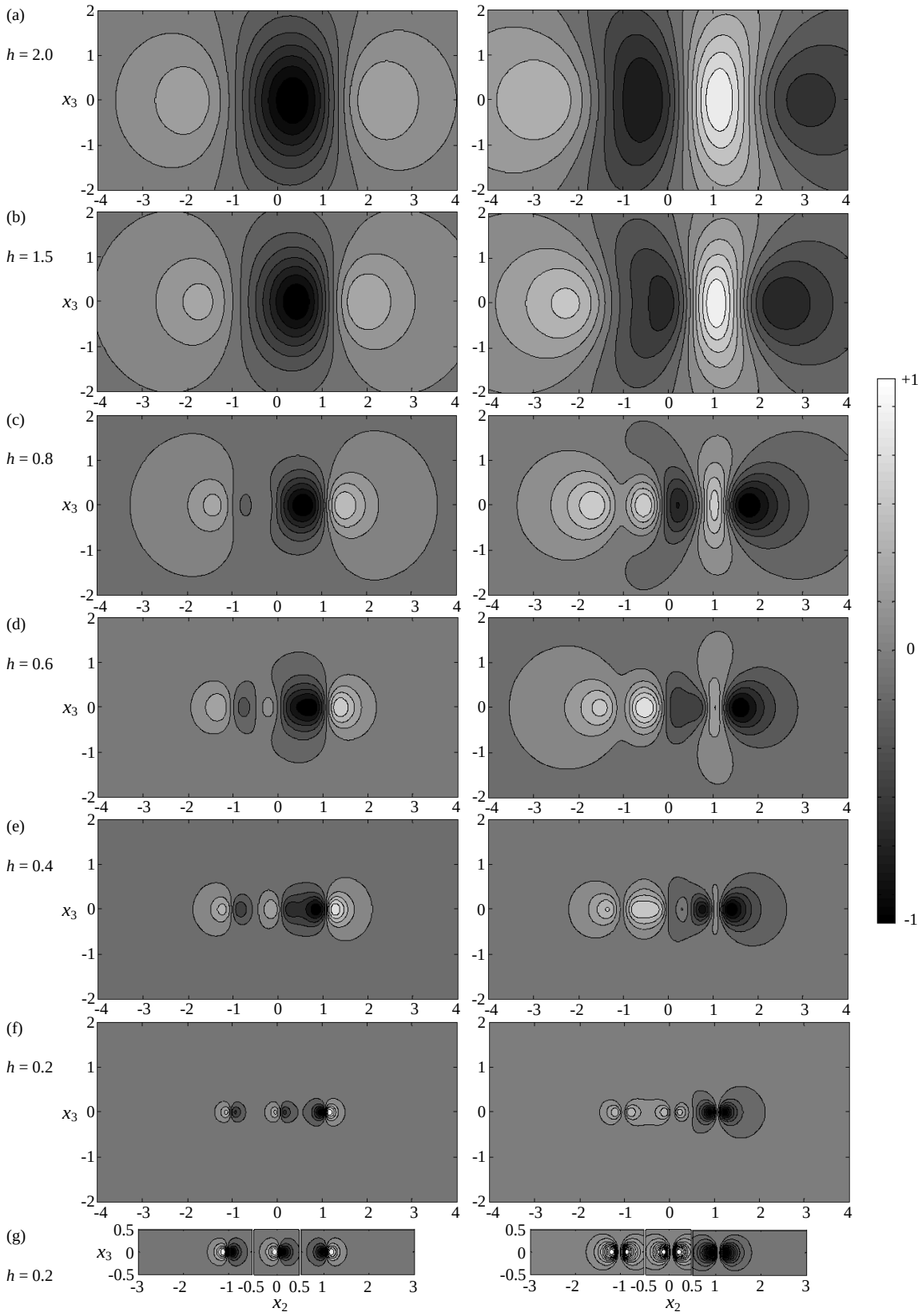

FIG. 4. The instantaneous traction in the x_1 direction (left) and in the x_2 direction (right) exerted by a three-sphere swimmer at $t = \pi/2$ when the (nondimensional) initial distance from the wall is (a) $h = 2.0$, (b) $h = 1.5$, (c) $h = 0.8$, (d) $h = 0.6$, (e) $h = 0.4$, and (f) $h = 0.2$. The instantaneous traction exerted by individual spheres at $h = 0.2$ is shown in (g). In each panel, the values are scaled by the largest magnitude traction in that panel.

The multipole expansion, however, is not suitable to describe a three-sphere swimmer close to the wall ($h < 2$). When the swimmer approaches the wall, distances from spheres to the image CM $\mathbf{x}^{0*}$ approaches similar magnitude to the image displacements $\mathbf{d}^{\beta*}$. As a result, our assumption for the multipole expansion breaks down. Instead, one must use the full expression for the velocity field which for our simple swimmer includes a separate Stokeslet for each sphere. For a more complicated swimmer, this corresponds to contributions to the velocity field which depend on the detailed internal structure and movement of parts of the swimmer rather than a far-field representation as a series of pointlike singularities.

As mentioned earlier, the wall-induced velocity can also be calculated using the wall traction approach. We verified that the wall traction approach yields the same results as the image approach by comparing $\mathbf{u}^*(\mathbf{x}^\alpha)$ obtained using Eq. 12 and Eq. 14 (data not shown). Here we examine the spatial pattern of the traction on the wall more closely. The traction on a fixed point $\mathbf{x}^{\mathrm{w}}$ due to the Blakeslet system of all the three spheres β can be written as,

$$T_i(\mathbf{x}^{\mathrm{w}}) = \sum_{\beta=1}^{3} \tau_{ij}(\mathbf{x}^{\mathrm{w}}, \mathbf{x}^\beta) f_j^\beta. \tag{16}$$

When the swimmer is placed far away from the wall, we are able to expand the traction expression above as,

$$T_i(\mathbf{x}^{\mathrm{w}}) = \sum_{\beta=1}^{3} \tau_{ij}(\mathbf{x}^{\mathrm{w}}, \mathbf{x}^0) f_j^\beta + \partial_k \tau_{ij}(\mathbf{x}^{\mathrm{w}}, \mathbf{x}^0) f_j^\beta d_k^\beta, \tag{17}$$

where the derivative is taken on the second argument of $\boldsymbol{\tau}$, and the displacement vector $\mathbf{d}^\beta = \mathbf{x}^\beta - \mathbf{x}^0$. The first and second terms represent the contribution of the Blakeslet and Blakeslet dipole, respectively. The force-free condition eliminates the first term in the expansion. We expect the multipole expansion for the velocity to be valid if and only if the expansion in Eq. 17 is valid for the traction. Hence, examining when the traction resembles that of a pure dipole should provide a way to gain a diagnosis of validity for the multipole expansion that does not require calculating the exact result. In FIG. 4 we plot the instantaneous traction exerted by the three-sphere swimmer at selected initial distance from the wall. For comparison, the Blakeslet dipole traction is plotted in FIG. 5a.

To quantify how much the traction due to the three-sphere swimmer differs from that expected from a far-field Blakeslet dipole, we analyse the spatial distribution of these two tractions using a traction correlation coefficient modified from the statistical 2-dimensional correlation coefficient. The traction correlation coefficient, R, is defined as

$$R = \frac{\int_S \frac{T_i T_i^{\mathrm{BD}}}{r^2} dS}{\sqrt{\left[\int_S \frac{T_i T_i}{r^2} dS\right] \left[\int_S \frac{T_i^{\mathrm{BD}} T_i^{\mathrm{BD}}}{r^2} dS\right]}}, \tag{18}$$

where T_i and T_i^{BD} are the spatial distribution of the traction in the i direction ($i = 1, 2, 3$) due to the swimmer and the Blakeslet dipole, respectively; $1/r$ is the reciprocal of the three-dimensional distance from the point on the wall to the CM of the swimmer/multipole, which takes into account the decay of the Blakeslet velocity from the traction point to the swimmer; S is the area of integration on the wall. $R = 0$ represents no correlation between the two tractions being compared while $R = -1$ and $R = +1$ represent prefect negative and positive correlation, respectively. We find that the correlation coefficient can be evaluated using S with linear dimension approximately one order of magnitude larger than h (details in Appendix D). Note that a correlation coefficient similar to Eq. 18 but without the $1/r$ factor yields similar results.

As seen from FIG. 5b, the correlation coefficient in both directions approaches 1 as h passes 0.8, and becomes close to 1 at $h \approx 2$ ($R\,|_{t=\pi/2} = 0.91$ and $R\,|_{t=3\pi/2} = 0.93$ at $h = 2.0$). The same conclusion can be drawn by visually examining the traction pattern: For $h > 2$, the traction pattern (FIG. 4a) resembles that of a pure dipole with force and displacement in the x_2 direction (FIG. 5a). This traction results from the far-field superposition of the tractions from all three spheres. As the swimmer approaches the wall, the internal structure of the swimmer becomes visible as individual contributions of the spheres become distinguishable and one can visually see that the traction becomes different from that of a pure dipole. We show this in FIG. 4 for decreasing h: at $h = 1.5$ (FIG. 4b) the traction has visible distortion, at $h = 0.8$ (FIG. 4c) hints of the influence of sphere 2 appear as an additional positive peak at $x_2 \approx -0.75$, at $h = 0.6$ (FIG. 4d) the influence of sphere 2 causes an additional positive peak at $x_2 \approx -0.25$ in the x_1 component of traction, at $h = 0.4$ (FIG. 4e) the right lobe of the traction of sphere 2 (FIG. 4g, middle panel) begins to be visible at $x_2 \approx 0.25$ in the x_2 component of traction and the left lobe is at $x_2 \approx -0.25$ in the x_1 component, and at $h = 0.2$ (FIG. 4f) the traction of all three spheres are clearly distinct.

In summary, because the dipole term is the first non-vanishing term of the multipole expansion, by calculating the correlation (Eq. 18) or visually examining whether the traction resembles that of a pure dipole one can determine at what distance from the boundary the far-field multipole expansion treatment of images becomes an accurate representation of the effect of the boundary on swimming. Note that for a swimmer with complex geometry, if the traction can be observed (experimentally or numerically, see discussion), this avoids the need for a numerical model to calculate the exact boundary traction

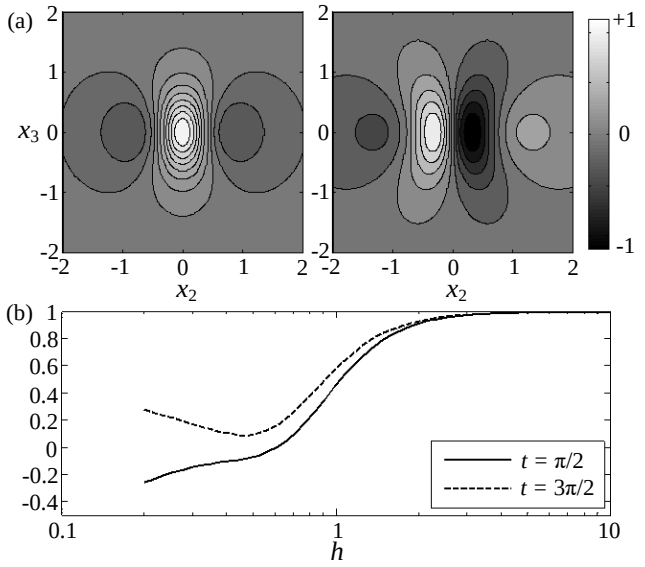

FIG. 5. (a) The traction plot in the x_1 direction (left) and in the x_2 direction (right) of a Blakeslet dipole when the only non-zero component of dipole strength is $f_2 d_2 = 1$. The dipole is placed at a (nondimensional) distance $h = 1$ from the wall. In each panel, the values are scaled by the largest magnitude traction in that panel. (b) Instantaneous traction correlation coefficient, which quantifies the correlation between the instantaneous traction due to the swimmer and a Stokeslet dipole with corresponding dipole strength $\sum_\beta \mathbf{f}^\beta \mathbf{d}^\beta$ at $t = \pi/2$ (solid line) and $t = 3\pi/2$ (dashed line).

and opens the door to justify the use of simplified models of boundary effects. In that regard, however, one should keep in mind that higher-order terms (but perhaps not too many) of the multipole expansion may be necessary to accurately find the velocity, as can already be seen in the example of the three-sphere swimmer we have investigated.

IV. TIME-AVERAGED RESPONSE

We have shown that traction patterns can be used to indicate when far-field approximations accurately represent boundary effects for instantaneous velocities. It has been suggested [55] that swimmers with a constant or time-averaged propulsion mechanism may have boundary effects that are different from those with time-varying strokes. We address this question by examining whether the traction approach could be used to correlate time-averaged traction with time-averaged swimming velocities. To proceed we first use the image system method to calculate the exact time-averaged velocity of a swimmer as a function of distance from the wall. We use angular brackets ($\langle\cdot\rangle$) to signify time averaging over one period of the swimming stroke.

Linear-log and absolute log-log plots of the x_2 component of the normalized wall-induced average velocity of the swimmer ($\langle u_2^*(\mathbf{x}^0)\rangle / \langle v^{0,\text{free}}\rangle$) as a function of h are shown in FIG. 6a and 6b (solid blue lines), respectively. When $h > 16.8$, the swimmer is sped up by the wall. For $h < 16.8$, the swimmer is slowed down by the wall. The change in sign of the boundary effect around $h = 16.8$ manifests as the negative divergence of the logarithm in FIG. 6b.

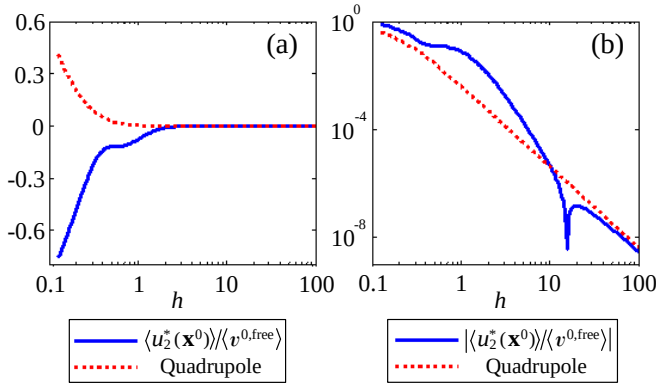

FIG. 6. (color online) (a) Semi-log and (b) absolute log-log scale of the normalized time-averaged wall-induced velocity of a three sphere swimmer in the x_2 direction $\langle u_2^*(\mathbf{x}^0)\rangle / \langle v^{0,\text{free}}\rangle$ (solid blue line) and a Stokeslet quadrupole model (dotted red line) versus the (nondimensional) initial distance from the wall.

At $h = 20$ (FIG. 7a), which is deep in the far-field, the traction appears to be nearly the same as that produced by a pure quadrupole near a boundary (FIG. 8a). This is consistent with the fact that due to the symmetry of the stroke, the time-averaged velocity field is quadrupolar, not dipolar [43]. Using this insight, we can model the effect of the wall on the swimming velocity by expressing it as the extra advection at the time-averaged CM location of the swimmer ($\overline{\mathbf{x}}^0$) due to the quadrupolar image system located at $\overline{\mathbf{x}}^{0*}$,

$$\langle u_i^*(\mathbf{x}^0)\rangle = \frac{1}{2}\sum_{\beta=1}^{3} \partial_l \partial_k St_{ij}(\overline{\mathbf{x}}^0, \overline{\mathbf{x}}^{0*}) \langle f_j^\beta d_k^{\beta*} d_l^{\beta*}\rangle, \qquad (19)$$

where $\mathbf{d}^{\beta*} = \mathbf{x}^{\beta*} - \overline{\mathbf{x}}^{0*}$ is now defined as the image displacement vector from the time-averaged image CM to image sphere β, and the derivatives act on the second argument of $\mathbf{St}$. The last term in brackets is the quadrupole strength. For $h > 16.8$, the change in velocity due to the boundary predicted by this model (FIG. 6, dotted red lines) agrees well with the actual wall-induced velocity (FIG. 6, solid blue lines).

It is apparent that for $h < 16.8$, the quadrupolar model of Eq. 19 does not do well. In fact, the quadrupolar model always predicts an increase in swimming speed of the swimmer, while for $h < 16.8$, the swimming speed is decreased by the wall, so the quadrupolar model is qualitatively inaccurate. However, if one examines the traction as h decreases, one finds that the traction pattern continues to resemble that of a pure quadrupole

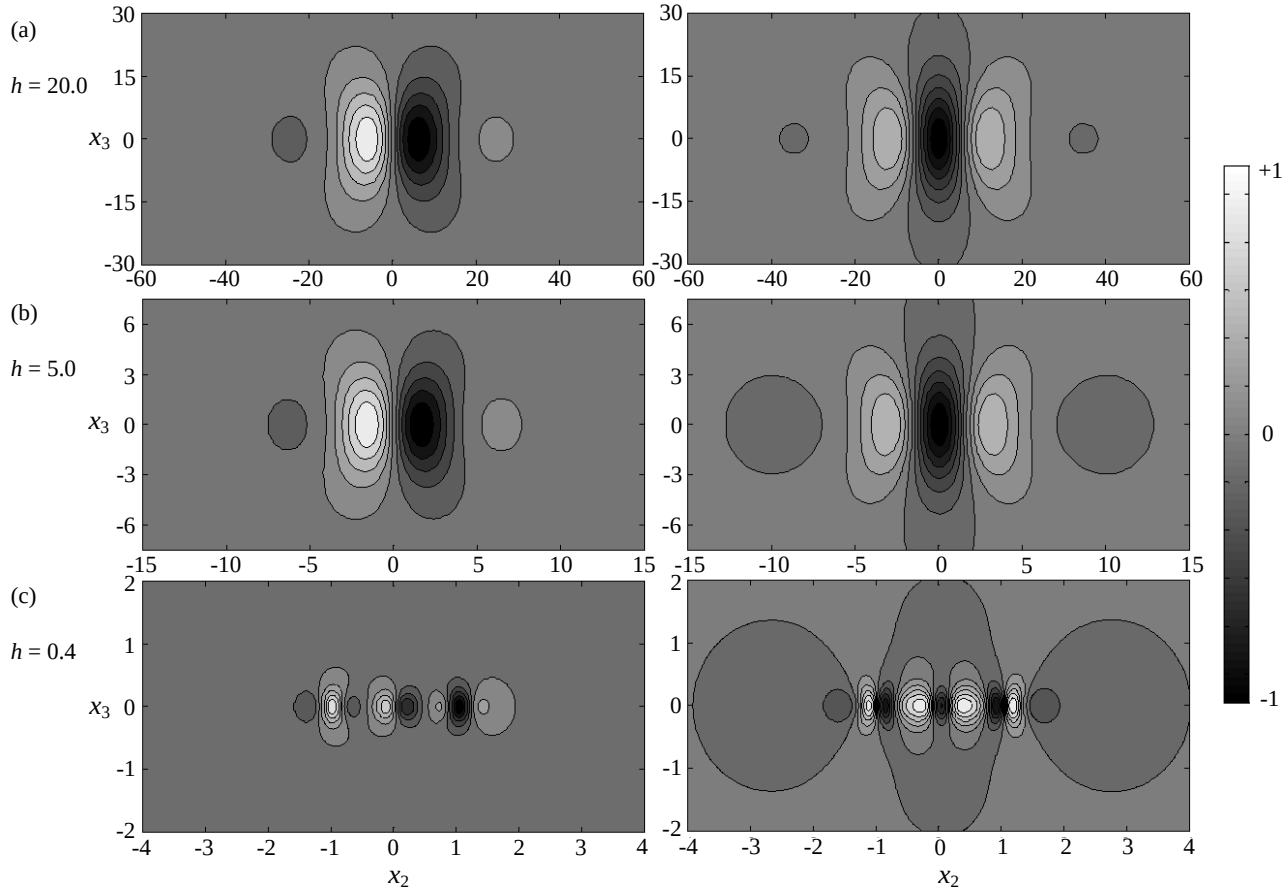

FIG. 7. The time-averaged traction in the x_1 direction (left) and in the x_2 direction (right) exerted by a three-sphere swimmer at the (nondimensional) initial distance from the wall (a) $h = 20.0$, (b) $h = 5.0$, and (c) $h = 0.4$. In each panel, the values are scaled by the largest magnitude traction in that panel.

until $h \approx 5$ (FIG. 7b). We adopt the same traction correlation coefficient analysis defined in Eq. 18 except using the time-averaged traction of the swimmer and the corresponding Blakeslet quadrupolar traction. As seen from FIG. 8b, it is only for $h \lesssim 2$ that the traction reveals signatures of the individual spheres, i.e. the internal structure of the swimmer in the near-field (e.g. FIG. 7c at $h = 0.4$). Thus, for time-averaged velocities, the traction does not seem to reflect the accuracy of a corresponding multipole model for the wall-induced velocity.

We can understand why one must be careful in connecting time-averaged tractions to time-averaged swimming velocities as follows. The wall-induced swimming velocity can be written as the average of the time-averaged wall-induced velocity over the three spheres:

$$\langle u_i^*(\mathbf{x}^0)\rangle = \frac{1}{3}\sum_{\alpha\beta}\langle St_{ij}(\mathbf{x}^\alpha, \mathbf{x}^{\beta *}) f_j^\beta\rangle. \tag{20}$$

In the far field, where $h \gg 1$, we can expand this as follows:

$$\begin{aligned}\langle u_i^*(\mathbf{x}^0)\rangle =& \frac{1}{3}\sum_{\alpha\beta} St_{ij}(\bar{\mathbf{x}}^0, \bar{\mathbf{x}}^{0*})\langle f_j^\beta\rangle \\ &+ \partial_k^{(2)} St_{ij}(\bar{\mathbf{x}}^0, \bar{\mathbf{x}}^{0*})\langle d_k^{\beta *} f_j^\beta\rangle \\ &+ \partial_k^{(1)} St_{ij}(\bar{\mathbf{x}}^0, \bar{\mathbf{x}}^{0*})\langle d_k^\alpha f_j^\beta\rangle \\ &+ \frac{1}{2}\partial_k^{(1)}\partial_l^{(1)} St_{ij}(\bar{\mathbf{x}}^0, \bar{\mathbf{x}}^{0*})\langle d_k^\alpha d_l^\alpha f_j^\beta\rangle \\ &+ \partial_k^{(1)}\partial_l^{(2)} St_{ij}(\bar{\mathbf{x}}^0, \bar{\mathbf{x}}^{0*})\langle d_k^\alpha d_l^{\beta *} f_j^\beta\rangle \\ &+ \frac{1}{2}\partial_k^{(2)}\partial_l^{(2)} St_{ij}(\bar{\mathbf{x}}^0, \bar{\mathbf{x}}^{0*})\langle d_k^{\beta *} d_l^{\beta *} f_j^\beta\rangle.\end{aligned} \tag{21}$$

where $\mathbf{d}^{\beta *} = \mathbf{x}^{\beta *} - \bar{\mathbf{x}}^{0*}$, $\mathbf{d}^\alpha = \mathbf{x}^\alpha - \bar{\mathbf{x}}^0$, while $\partial^{(1)}$ and $\partial^{(2)}$ denote derivatives taken with respect to the first and second argument of $\mathbf{St}$, respectively. The last term in this expression gives the quadrupolar model. While the first and second term involve the total average force on the swimmer and the average dipole of the swimmer, respectively, and hence vanish, the averages in the third term do not vanish in general. These

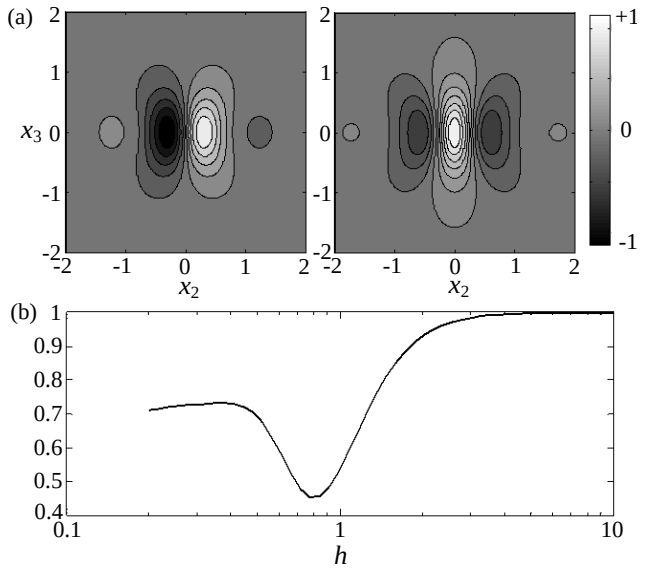

FIG. 8. (a) The traction plot in the x_1 direction (left) and in the x_2 direction (right) of a Blakeslet quadrupole when the only non-zero component of quadrupole strength is $f_2 d_2 d_2 = 1$. The quadrupole is placed at a (nondimensional) distance $h = 1$ from the wall. In each panel, the values are scaled by the largest magnitude traction in that panel. (b) Traction correlation coefficient quantifying the correlation between the time-averaged traction due to the swimmer and a Stokeslet quadrupole with corresponding quadrupolar strength $\sum_\beta \mathbf{f}^\beta \mathbf{d}^\beta \mathbf{d}^\beta$.

averages capture the correlation between the motion of the spheres and the hydrodynamic influence of one sphere on another, which are crucial to correctly determining average swimming speeds. On the other hand, the time-averaged traction is evaluated at a fixed point on the boundary (See Eq. 13), hence cannot capture these correlations, and provides an inaccurate picture of the contributions to the time-averaged wall-induced velocity. We conclude that while the instantaneous traction is useful to understand when far-field models will be accurate representations for the effects of boundaries on instantaneous swimming speeds, one must be more careful about using time-averaged traction to make conclusions about time-averaged swimming speeds.

V. DISCUSSION

We have investigated the effect of a boundary on a three-sphere swimmer to exemplify the use of wall tractions for understanding boundary effects. For instantaneous swimming velocities, the boundary effect on the swimming velocity of the three-sphere swimmer is first calculated using the image system method, which allowed us to establish the limits of validity of a multipole representation of the boundary effects. We show that the range of validity of the multipole representation can be independently be diagnosed by comparing the wall traction to that of a pure multipole, either using a correlation coefficient or by visual inspection. When the wall traction is dissimilar to that of a pure multipole, the multipole representation is not valid and the inner structure of the swimmer is important for the swimmer-boundary interaction. However, we find that one should be cautious when using the time-averaged traction to draw conclusions about the validity of multipole approximations for boundary effects on time-averaged swimming speeds. Although the three-sphere swimmer is rather simple, it is a clear realization of a swimmer that, like many biological swimmers, has near-field velocity fields that are quite different from a far-field multipole representation. Thus, we expect that the insights gained can be applied to similar transitions in the validity of multipole expansions for more realistic swimmers compared to models that incorporate near-field details.

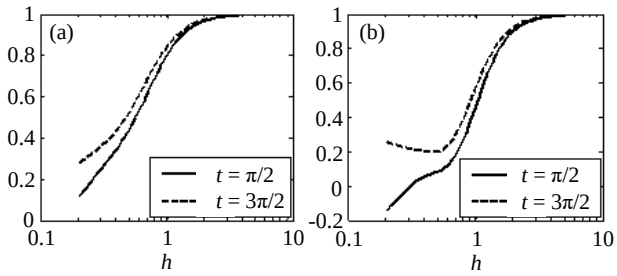

FIG. 9. (a) Velocity correlation coefficient and (b) Stress correlation coefficient quantifying the correlation between the unbounded swimmer and a Stokeslet dipole at $t = \pi/2$ (solid lines) and $t = 3\pi/2$ (dashed lines).

This work has some practical use since it demonstrates an independent way to find the limit of validity of the multipole representation for boundary effects. For numerical calculations, we can leverage our findings to determine whether the multipole representation of boundary effects is valid without having to do a full calculation of the boundary effects including near-field details, which was not possible in previous approaches [55]. Our results suggest that simply analysing the correlation between the velocity field for an unconfined swimmer and the corresponding multipole expansion is enough to make conclusions about the range of validity of using the multipole expansion for boundary effects. To test this, we have analysed the velocity and stress fields due to an unbounded three-sphere swimmer on an imaginary plane parallel to the axis of the swimmer. Using a correlation coefficient similar to Eq. 18, but in the absence of a boundary, we determine how far away from the swimmer the stress/velocity field of the swimmer is similar to multipole-like stress/velocity field. When the distance from the swimmer to the imaginary plane is more than $2L$, the unbounded swimmer behaves like a Stokeslet dipole (Velocity: $R\,|_{t=\pi/2} = 0.97$ and $R\,|_{t=3\pi/2} = 0.97$; Stress: $R\,|_{t=\pi/2} = 0.91$ and $R\,|_{t=3\pi/2} =$

0.93) (FIG. 9). Therefore, even without calculating full boundary effects, one could diagnose whether to use images of a detailed discretization or of an image multipole to treat boundary effects accurately in a computation.

Experimentally, one could apply our results and test the correlation of the wall traction with that of a pure multipole by using traction force microscopy (TFM) [58] to directly measure the wall traction near a swimmer. In short, the forces on the boundary are quantified by the deformation of a thin layer ($\sim$ 20 μm) of substrate on glass slides, and the strain on substrate is quantified through tracking the lateral displacement of nanoscale fiducial markers embedded in the substrate. TFM can measure the magnitude of the deformation down to tens of nanometers at submicrometer spatial resolution [59, 60] corresponding to nanoNewtons of force. However, note that if the frequency of the swimming stroke is higher than or in the same order of the microscopy video frequency, TFM can only capture the time-averaged traction due to the microswimmer, resulting in qualitative conclusion of the wall traction approach. Experiments on traction measurement could be feasible for pelagic crustaceans with characteristic length up to several millimeters but would be technically challenging for microscale microswimmers. Following the observations made in the previous paragraph, an additional experimental way to apply our results is to measure velocity fields of freely swimming microorganisms away from boundaries via particle image velocimetry (PIV) and compare those to pure multipoles, which can be achieved for microorganisms as small as *Chlamydomonas* (10-30 μm) [37, 61]. The results would indicate whether models of wall-effects on swimming behavior require detailed treatments of near-field hydrodynamics or could use simplified multipole representations.

Appendix A: Image system method

The fundamental solution of the Stokes Equation at low Reynolds number is the Stokeslet, or the velocity at an arbitrary point $\mathbf{x}^{\mathrm{p}}$ due to a point force $\mathbf{f}$ acting at $\mathbf{x}^0$ [28],

$$u_i^{\mathrm{s}}(\mathbf{x}^{\mathrm{p}}) = S_{ij}(\mathbf{x}^{\mathrm{p}}, \mathbf{x}^0) f_j, \tag{A1}$$

where the Stokeslet kernel $S_{ij} = \frac{\delta_{ij}}{8\pi r} + \frac{(x_i^{\mathrm{p}} - x_i^0)(x_j^{\mathrm{p}} - x_j^0)}{8\pi r^3}$, and $r = [(x_i^{\mathrm{p}} - x_i^0)(x_i^{\mathrm{p}} - x_i^0)]^{\frac{1}{2}}$.

The method of images for a Stokeslet is commonly used to satisfy the no-slip boundary condition of an infinite planar wall at $x_1 = 0$ (FIG. 10) [54]. The entire space above the wall is filled with viscous fluid, and a Stokeslet $\mathbf{f} = (f_1, f_2, f_3)$ is placed at $\mathbf{x}^0 = (h, x_2, x_3)$, where h is the distance to the wall. A set of singular images consisting of an image Stokeslet, a potential dipole and a Stokeslet doublet are placed at the image location $\mathbf{x}^{0*}$ such that

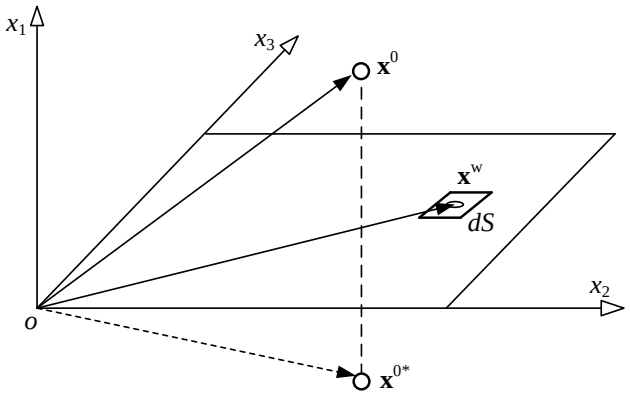

FIG. 10. A Stokeslet at $\mathbf{x}^0$ and its image system at $\mathbf{x}^{0*}$ with the infinite wall located at $x_1 = 0$ plane. An infinitesimal area dS on the wall is centered at $\mathbf{x}^{\mathrm{w}}$.

$\mathbf{x}^{0*} = \mathbf{x}^0 - 2\left(\mathbf{x}^0 \cdot \mathbf{n}\right)\mathbf{n}$, where $\mathbf{n} = (1, 0, 0)$ is the unit vector perpendicular to the wall. Thus, the velocity of a point $\mathbf{x}^{\mathrm{p}}$ due to the image system of a Stokeslet, named as the wall-induced velocity $\mathbf{u}^*(\mathbf{x}^{\mathrm{p}})$, is

$$u_i^*(\mathbf{x}^{\mathrm{p}}) = u_i^{\mathrm{s}*}(\mathbf{x}^{\mathrm{p}}) + u_i^{\mathrm{pd}}(\mathbf{x}^{\mathrm{p}}) + u_i^{\mathrm{sd}}(\mathbf{x}^{\mathrm{p}}), \tag{A2}$$

where

$$u_i^{\mathrm{s}*}(\mathbf{x}^{\mathrm{p}}) = S_{ij}(\mathbf{x}^{\mathrm{p}}, \mathbf{x}^{0*})(-f_j), \tag{A3}$$

$$u_i^{\mathrm{pd}}(\mathbf{x}^{\mathrm{p}}) = \frac{q_i}{4\pi r^{*3}} - \frac{3q_j(x_j^{\mathrm{p}} - x_j^{0*})(x_i^{\mathrm{p}} - x_i^{0*})}{4\pi r^{*5}}, \tag{A4}$$

$$\begin{aligned} u_i^{\mathrm{sd}}(\mathbf{x}^{\mathrm{p}}) =& \frac{n_j g_j (x_i^{\mathrm{p}} - x_i^{0*}) + n_j (x_j^{\mathrm{p}} - x_j^{0*}) g_i}{8\pi r^{*3}} \\ &- \frac{g_j (x_j^{\mathrm{p}} - x_j^{0*}) n_i}{8\pi r^{*3}} \\ &- \frac{3 n_j (x_j^{\mathrm{p}} - x_j^{0*}) g_k (x_k^{\mathrm{p}} - x_k^{0*})(x_i^{\mathrm{p}} - x_i^{0*})}{8\pi r^{*5}}, \end{aligned} \tag{A5}$$

$\mathbf{q} = -h^2\left[2\left(\mathbf{f}\cdot\mathbf{n}\right)\mathbf{n} - \mathbf{f}\right]$, $\mathbf{g} = 2h\left[2\left(\mathbf{f}\cdot\mathbf{n}\right)\mathbf{n} - \mathbf{f}\right]$ and $r^* = \left[(x_i^{\mathrm{p}} - x_i^{0*})(x_i^{\mathrm{p}} - x_i^{0*})\right]^{\frac{1}{2}}$. The superscript s*, sd and pd correspond to the image Stokeslet, the Stokeslet dipole and the potential dipole, respectively. For simplicity, since both $\mathbf{q}$ and $\mathbf{g}$ are functions of $\mathbf{f}$, we define $\mathbf{St}$ using

$$u_i^*(\mathbf{x}^{\mathrm{p}}) = St_{ij}(\mathbf{x}^{\mathrm{p}}, \mathbf{x}^{0*}) f_j, \tag{A6}$$

where $\mathbf{f}$ is the strength of a Stokeslet so that $\mathbf{St}$ is the kernel of the image system of the Stokeslet, which only depends on the position of the Stokeslet's image system $\mathbf{x}^{0*}$ and the evaluation point $\mathbf{x}^{\mathrm{p}}$. Incorporating the contribution of the original Stokeslet with its images, the net velocity due to a Blakeslet can be expressed as $\mathbf{v}\left(\mathbf{x}^{\mathrm{p}}\right) = \mathbf{u}^s\left(\mathbf{x}^{\mathrm{p}}\right) + \mathbf{u}^*\left(\mathbf{x}^{\mathrm{p}}\right)$, or

$$v_i(\mathbf{x}^{\mathrm{p}}) = [S_{ij}(\mathbf{x}^{\mathrm{p}}, \mathbf{x}^0) + St_{ij}(\mathbf{x}^{\mathrm{p}}, \mathbf{x}^{0*})] f_j. \tag{A7}$$

Appendix B: Wall traction approach

An alternative approach to find $\mathbf{u}^*(\mathbf{x}^{\mathrm{p}})$ due to a single Blakeslet is to utilize a boundary integral representation of the flow due to the traction distribution on the wall. We refer this approach as the wall traction approach. The stress at any point in the flow $\mathbf{x}^{\mathrm{p}}$ is

$$\sigma_{ij}(\mathbf{x}^{\mathrm{p}}) = -p(\mathbf{x}^{\mathrm{p}})I_{ij} + \frac{\partial u_i(\mathbf{x}^{\mathrm{p}})}{\partial x_j} + \frac{\partial u_j(\mathbf{x}^{\mathrm{p}})}{\partial x_i}, \tag{B1}$$

where $\mathbf{I}$ is an identity matrix, $p(\mathbf{x}^{\mathrm{p}})$ and $\mathbf{u}(\mathbf{x}^{\mathrm{p}})$ are the pressure and velocity at $\mathbf{x}^{\mathrm{p}}$.

The velocity at $\mathbf{x}^{\mathrm{p}}$ due to a Stokeslet, an image Stokeslet, a potential dipole and a Stokeslet dipole are shown in Eq. A1 and Eqs. A3 - A5, respectively. The corresponding pressure fields are given by,

$$p^{\mathrm{s}}(\mathbf{x}^{\mathrm{p}}) = -\frac{f_j(x_j^{\mathrm{p}} - x_j^0)}{4\pi r^3}, \tag{B2}$$

$$p^{\mathrm{s}*}(\mathbf{x}^{\mathrm{p}}) = -\frac{(-f_j)(x_j^{\mathrm{p}} - x_j^{0*})}{4\pi r^{*3}}, \tag{B3}$$

$$p^{\mathrm{pd}}(\mathbf{x}^{\mathrm{p}}) = 0, \tag{B4}$$

$$p^{\mathrm{sd}}(\mathbf{x}^{\mathrm{p}}) = -\frac{n_i g_i}{4\pi r^{*3}} + 3\frac{n_i(x_i^{\mathrm{p}} - x_i^{0*})g_j(x_j^{\mathrm{p}} - x_j^{0*})}{4\pi r^{*5}}. \tag{B5}$$

The overall traction on any infinitesimal area dS on the wall centered at $\mathbf{x}^{\mathrm{w}}$ due to a Blakeslet is the net effect of the original Stokeslet itself located at $\mathbf{x}^0$ and its image system located at $\mathbf{x}^{0*}$. By setting $\mathbf{x}^{\mathrm{p}} = \mathbf{x}^{\mathrm{w}}$, the traction at $\mathbf{x}^{\mathrm{w}}$ due to a Blakeslet can be expressed as,

$$T_i(\mathbf{x}^{\mathrm{w}}) = \left[\sigma_{ij}^{\mathrm{s}}(\mathbf{x}^{\mathrm{w}}) + \sigma_{ij}^{\mathrm{s}*}(\mathbf{x}^{\mathrm{w}}) + \sigma_{ij}^{\mathrm{pd}}(\mathbf{x}^{\mathrm{w}}) + \sigma_{ij}^{\mathrm{sd}}(\mathbf{x}^{\mathrm{w}})\right] n_j, \tag{B6}$$

or,

$$T_i(\mathbf{x}^{\mathrm{w}}) = T_i^{\mathrm{s}}(\mathbf{x}^{\mathrm{w}}) + T_i^{\mathrm{s}*}(\mathbf{x}^{\mathrm{w}}) + T_i^{\mathrm{pd}}(\mathbf{x}^{\mathrm{w}}) + T_i^{\mathrm{sd}}(\mathbf{x}^{\mathrm{w}}), \tag{B7}$$

where,

$$T_i^{\mathrm{s}}(\mathbf{x}^{\mathrm{w}}) = -\frac{3n_j(x_j^{\mathrm{w}} - x_j^0)f_k(x_k^{\mathrm{w}} - x_k^0)(x_i^{\mathrm{w}} - x_i^0)}{4\pi r^5}, \tag{B8}$$

$$T_i^{\mathrm{s}*}(\mathbf{x}^{\mathrm{w}}) = -\frac{3n_j(x_j^{\mathrm{w}} - x_j^{0*})(-f_k)(x_k^{\mathrm{w}} - x_k^{0*})(x_i^{\mathrm{w}} - x_i^{0*})}{4\pi r^{*5}}, \tag{B9}$$

$$\begin{aligned} T_i^{\mathrm{pd}}(\mathbf{x}^{\mathrm{w}}) = &-3\frac{q_j(x_j^{\mathrm{w}} - x_j^{0*})n_i + n_j q_j(x_i^{\mathrm{w}} - x_i^{0*})}{2\pi r^{*5}} \\ &- \frac{3n_j(x_j^{\mathrm{w}} - x_j^{0*})q_i}{2\pi r^{*5}} \\ &+ \frac{15n_j(x_j^{\mathrm{w}} - x_j^{0*})q_k(x_k^{\mathrm{w}} - x_k^{0*})(x_i^{\mathrm{w}} - x_i^{0*})}{2\pi r^{*7}}, \end{aligned} \tag{B10}$$

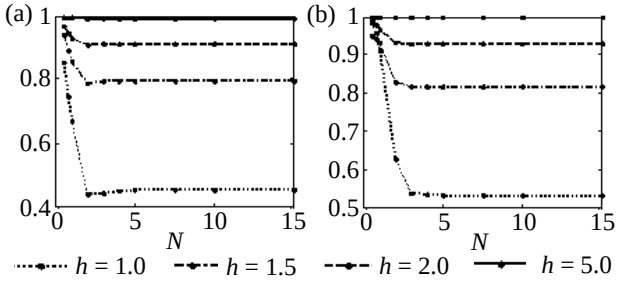

FIG. 11. (a) Instantaneous ($t = \pi/2$) and (b) time-averaged traction correlation coefficient by varying the square of side length Nh on the wall.

$$\begin{aligned} T_i^{\mathrm{sd}}(\mathbf{x}^{\mathrm{w}}) = &-\frac{3n_j(x_j^{\mathrm{w}} - x_j^{0*})n_k g_k(x_i^{\mathrm{w}} - x_i^{0*})}{2\pi r^{*5}} \\ &- \frac{3\left[n_j(x_j^{\mathrm{w}} - x_j^{0*})\right]^2 g_i}{4\pi r^{*5}} \\ &+ \frac{15\left[n_j(x_j^{\mathrm{w}} - x_j^{0*})\right]^2 g_k(x_k^{\mathrm{w}} - x_k^{0*})(x_i^{\mathrm{w}} - x_i^{0*})}{4\pi r^{*7}}. \end{aligned} \tag{B11}$$

The traction expressed in Eq. B7 is linear in the force so it can be written as

$$T_i(\mathbf{x}^{\mathrm{w}}) = \tau_{ij}(\mathbf{x}^{\mathrm{w}}, \mathbf{x}^0)f_j. \tag{B12}$$

Viewing the traction as a distribution of Stokeslets on the wall, we are able to evaluate the wall-induced velocity on any arbitrary point $\mathbf{x}^{\mathrm{p}}$ through

$$u_i^*(\mathbf{x}^{\mathrm{p}}) = \int_S S_{ij}\left(\mathbf{x}^{\mathrm{p}}, \mathbf{x}^{\mathrm{w}}\right) T_j\left(\mathbf{x}^{\mathrm{w}}\right) dS. \tag{B13}$$

Appendix C: Multipole tractions

The Blakeslet dipolar and Blakeslet quadrupolar traction on a fixed point $\mathbf{x}^{\mathrm{w}}$ can be obtained by differentiating Eq. B12,

$$T_i^D(\mathbf{x}^{\mathrm{w}}) = \partial_k \tau_{ij}(\mathbf{x}^{\mathrm{w}}, \mathbf{x}^0)f_j d_k, \tag{C1}$$

$$T_i^Q(\mathbf{x}^{\mathrm{w}}) = \partial_k \partial_l \tau_{ij}(\mathbf{x}^{\mathrm{w}}, \mathbf{x}^0)f_j d_k d_l, \tag{C2}$$

where the derivatives act on the second argument of $\boldsymbol{\tau}$. The Blakeslet dipolar traction when the only non-zero dipolar strength component is $f_2 d_2 = 1$ is shown in FIG. 5a while the Blakeslet quadrupolar traction when the only non-zero quadrupolar strength component is $f_2 d_2 d_2 = 1$ is shown in FIG. 8a. Both singularities are placed at a distance of $h = 1$ from the wall.

Appendix D: Traction correlation coefficient

Following the traction correlation coefficient defined in Eq. 18, convergence tests are performed to determine

how large the sample area on the wall must be to find correlation coefficients that do not depend on the integration area size. Here we show the result for the instantaneous traction at $t = \pi/2$ and the time-averaged traction. The same method can be extended to study the instantaneous traction at other time points (data not shown).

We define the total area to be examined as a square centered on the projection of CM of the swimmer on the x_2-x_3 plane. The square has a side length of Nh. We evaluate R numerically for the traction due to the three-sphere swimmer and the corresponding Stokeslet dipole with strength $\sum_\beta \mathbf{f}^\beta \mathbf{d}^\beta$ using Eq. 18, plot against N (FIG. 11). For a given h, the correlation coefficients in both x_1 and x_2 directions converge when the side length of the area being examined is approximately 3-5 times larger than the distance from the wall to the three-sphere swimmer ($N \gtrsim$ 3-5), and certainly for all cases when $N \gtrsim 10$.

[1] C. A. Suttle, Nature Rev. Microbiol. **5**, 801 (2007).
[2] M. E. Cortés, J. Consuegra, and R. D. Sinisterra, Sci. Microb. Pathog. Commun. Curr. Res. Technol. Adv. **2**, 896 (2011).
[3] M. R. Amieva and E. M. El-Omar, Gastroenterology **134**, 306 (2008).
[4] R. M. Macnab, P. Natl. Acad. Sci. USA **74**, 221 (1977).
[5] J. Gray, J. Exp. Biol. **32**, 775 (1955).
[6] Marcos, N. P. Tran, A. R. Saini, K. C. H. Ong, and W. J. Chia, Microfluid. Nanofluid. **17**, 809 (2014).
[7] J. B. Y. Koh and Marcos, Microfluid. Nanofluid. **18**, 755 (2015).
[8] Y. Wang, R. M. Hernandez, D. J. Bartlett, J. M. Bingham, T. R. Kline, A. Sen, and T. E. Mallouk, Langmuir **22**, 10451 (2006).
[9] A. Ghosh and P. Fischer, Nano lett. **9**, 2243 (2009).
[10] L. Zhang, J. J. Abbott, L. Dong, B. E. Kratochvil, D. Bell, and B. J. Nelson, Appl. Phys. Lett. **94**, 064107 (2009).
[11] D. L. Fan, F. Q. Zhu, R. C. Cammarata, and C. L. Chien, Nano Today **6**, 339 (2011).
[12] S. Kim, F. Qiu, S. Kim, A. Ghanbari, C. Moon, L. Zhang, B. J. Nelson, and H. Choi, Adv. Mater. **25**, 5863 (2013).
[13] U. K. Cheang, F. Meshkati, D. Kim, M. J. Kim, and H. C. Fu, Phys. Rev. E **90**, 033007 (2014).
[14] A. Ferreira, J. Agnus, N. Chaillet, and J.-M. Breguet, IEEE-ASME T. Mech. **9**, 508 (2004).
[15] F. Meshkati and H. C. Fu, Phys. Rev. E **90**, 063006 (2014).
[16] H. C. Fu, M. Jabbarzadeh, and F. Meshkati, Phys. Rev. E **91**, 043011 (2015).
[17] F. K. Nelson and D. L. Riddle, J. Exp. Zoo **231**, 45 (1984).
[18] J. Edd, S. Payen, B. Rubinsky, M. L. Stoller, and M. Sitti, in *Proc. IEEE/RSJ Int. Conf. Intell. Robots Syst.*, Vol. 3 (IEEE, 2003) pp. 2583–2588.
[19] G. Dogangil, O. Ergeneman, J. J. Abbott, S. Pané, H. Hall, S. Muntwyler, and B. J. Nelson, in *Proc. IEEE/RSJ Int. Conf. Intell. Robots Syst.* (IEEE, 2008) pp. 1921–1926.
[20] S. Fusco, G. Chatzipirpiridis, K. M. Sivaraman, O. Ergeneman, B. J. Nelson, and S. Pané, Adv. Healthc. Mater. **2**, 1037 (2013).
[21] G. Taylor, in *Proc. R. Soc. A*, Vol. 209 (The Royal Society, 1951) pp. 447–461.
[22] H. C. Fu, V. B. Shenoy, and T. R. Powers, Europhys. Lett. **91**, 24002 (2010).
[23] S. A. Mirbagheri and H. C. Fu, Phys. Rev. Lett. **116**, 198101 (2016).
[24] E. M. Purcell, Am. J. Phys. **45**, 3 (1977).
[25] A. Najafi and R. Golestanian, Phys. Rev. E **69**, 062901 (2004).
[26] M. Jabbarzadeh, Y. K. Hyon, and H. C. Fu, Phys. Rev. E **90**, 043021 (2014).
[27] J. E. Avron, O. Kenneth, and D. H. Oaknin, New J. Phys. **7**, 234 (2005).
[28] S. Kim and S. J. Karrila, *Microhydrodynamics: principles and selected applications* (Butterworth-Heinemann, Boston, 1991).
[29] J. Lighthill, SIAM Rev. **18**, 161 (1976).
[30] J. B. Y. Koh, X. Shen, and Marcos, Microfluid. Nanofluid. **20**, 98 (2016).
[31] M. Ramia, D. L. Tullock, and N. Phan-Thien, Biophys. J. **65**, 755 (1993).
[32] R. Cortez, SIAM J. Sci. Comput. **23**, 1204 (2001).
[33] R. Cortez, L. Fauci, and A. Medovikov, Phys. Fluids **17**, 031504 (2005).
[34] Y. Hyon, Marcos, T. R. Powers, R. Stocker, and H. C. Fu, J. Fluid Mech. **705**, 58 (2012).
[35] T. D. Montenegro-Johnson, D. A. Gagnon, P. E. Arratia, and E. Lauga, Phys. Rev. Fluids **1**, 053202 (2016).
[36] J. D. Martindale, M. Jabbarzadeh, and H. C. Fu, Phys. Fluids **28**, 021901 (2016).
[37] K. Drescher, R. E. Goldstein, N. Michel, M. Polin, and I. Tuval, Phys. Rev. Lett. **105**, 168101 (2010).
[38] A. Visser, Mar. Ecol-Prog. Ser. **222**, 1 (2001).
[39] G. K. Batchelor, J. Fluid Mech. **41**, 545 (1970).
[40] T. Ishikawa, G. Sekiya, Y. Imai, and T. Yamaguchi, Biophys. J. **93**, 2217 (2007).
[41] E. Lauga and T. R. Powers, Rep. Prog. Phys. **72**, 096601 (2009).
[42] D. J. Smith and J. R. Blake, Math. Scientist **34** (2009).
[43] C. Pooley, G. Alexander, and J. Yeomans, Soft Condens. Matter (2007).
[44] E. Lauga, W. R. DiLuzio, G. M. Whitesides, and H. A. Stone, Biophys. J. **90**, 400 (2006).
[45] P. Tierno, R. Golestanian, I. Pagonabarraga, and F. Sagués, Phys. Rev. Lett. **101**, 218304 (2008).
[46] H. Shum, E. A. Gaffney, and D. J. Smith, in *Proc. R. Soc. A*, Vol. 466 (The Royal Society, 2010) pp. 1725–1748.
[47] L. Lemelle, J.-F. Palierne, E. Chatre, C. Vaillant, and C. Place, Soft Matter **9**, 9759 (2013).
[48] N. Figueroa-Morales, G. L. Miño, A. Rivera, R. Caballero, E. Clément, E. Altshuler, and A. Lindner, Soft Matter **11**, 6284 (2015).
[49] L. Ping, V. Wasnik, and E. Emberly, FEMS Microbiol. Ecol. **91**, 1 (2015).
[50] A. P. Berke, L. Turner, H. C. Berg, and E. Lauga, Phys.

Rev. Lett. **101**, 038102 (2008).
[51] G.-J. Li and A. M. Ardekani, Phys. Rev. E **90**, 013010 (2014).
[52] K. Ishimoto and E. A. Gaffney, Phys. Rev. E **88**, 062702 (2013).
[53] A. J. T. M. Mathijssen, D. O. Pushkin, and J. M. Yeomans, J. Fluid Mech. **773**, 498 (2015).
[54] J. R. Blake and A. T. Chwang, J. Eng. Math. **8**, 23 (1974).
[55] S. E. Spagnolie and E. Lauga, J. Fluid Mech. **700**, 105 (2012).
[56] C. Pozrikidis, *Boundary integral and singularity methods for linearized viscous flow* (Cambridge University Press, 1992).
[57] R. Zargar, A. Najafi, and M. F. Miri, Phys. Rev. E **80**, 026308 (2009).
[58] A. K. Harris, P. Wild, D. Stopak, *et al.*, Science **208**, 177 (1980).
[59] B. Sabass, M. L. Gardel, C. M. Waterman, and U. S. Schwarz, Biophys. J. **94**, 207 (2008).
[60] H. Colin-York, D. Shrestha, J. H. Felce, D. Waithe, E. Moeendarbary, S. J. Davis, C. Eggeling, and M. Fritzsche, Nano lett. **16**, 2633 (2016).
[61] J. S. Guasto, K. A. Johnson, and J. P. Gollub, Phys. Rev. Lett. **105**, 168102 (2010).